Interior tomographic imaging of mouse heart in a carbon nanotube micro-CT

Hao Gong[a], Rui Liu[b,c], Hengyong Yu[c], Jianping Lu[d], Otto Zhou[d], Lijuan Kan[e], Jia-Qiang He[e] and Guohua Cao[a,*]

[a]*Department of Biomedical Engineering and Mechanics, Virginia Polytechnic Institute and State University, Blacksburg, VA, USA*

[b]*Virginia Tech-Wake Forest School of Biomedical Engineering and Science, Wake Forest University Health Sciences, Winston-Salem, NC, USA*

[c]*Department of Electrical and Computer Engineering, University of Massachusetts Lowell, Lowell, MA, USA*

[d]*Department of Physics and Astronomy, University of North Carolina at Chapel Hill, Chapel Hill, NC, USA*

[e]*Department of Biomedical Sciences and Pathobiology, Virginia-Maryland College of Veterinary Medicine, Virginia Polytechnic Institute and State University, VA, USA*

Received 10 August 2015
Revised 26 February 2016
Accepted 27 March 2016

Abstract.
BACKGROUND: The relatively high radiation dose from micro-CT is a cause for concern in preclinical research involving animal subjects. Interior region-of-interest (ROI) imaging was proposed for dose reduction, but has not been experimentally applied in micro-CT.
OBJECTIVE: Our aim is to implement interior ROI imaging in a carbon nanotube (CNT) x-ray source based micro-CT, and present the ROI image quality and radiation dose reduction for interior cardiac micro-CT imaging of a mouse heart *in situ*.
METHODS: An aperture collimator was mounted at the source-side to induce a small-sized cone beam (10 mm width) at the isocenter. Interior *in situ* micro-CT scans were conducted on a mouse carcass and several micro-CT phantoms. A GPU-accelerated hybrid iterative reconstruction algorithm was employed for volumetric image reconstruction. Radiation dose was measured for the same system operated at the interior and global micro-CT modes.
RESULTS: Visual inspection demonstrated comparable image quality between two scan modes. Quantitative evaluation demonstrated high structural similarity index (up to 0.9614) with improved contrast-noise-ratio (CNR) on interior micro-CT mode. Interior micro-CT mode yielded significant reduction (up to 83.9%) for dose length product (DLP).
CONCLUSIONS: This work demonstrates the applicability of using CNT x-ray source based interior micro-CT for preclinical imaging with significantly reduced radiation dose.

Keywords: Micro-CT, interior tomography, carbon-nanotube x-ray micro-CT

*Corresponding author: Guohua Cao, Department of Biomedical Engineering and Mechanics, Virginia Polytechnic Institute and State University, Blacksburg, VA 24061, USA. Tel.: +540 2315686; Fax: +540 231 0970; E-mail: ghcao@vt.edu.

1. Introduction

Mouse models of human diseases have been widely used in preclinical studies [1–4]. Micro-CT provides biomedical researchers with low-cost, high-throughput, high-resolution and non-invasive evaluation of anatomical structure and physiological function [5]. However, high radiation dose is often required to generate high-resolution micro-CT images [6]. The radiation dose is estimated to be inversely scaled with the fourth power of image voxel size in order to maintain the same image noise level [6, 7]. Both high-dose radiation exposure [8, 9] and longitudinal low-dose radiation exposure [10, 11] could induce a variety of pathological effects to small animals and perturb the experimental outcomes. The radiation-induced biological effects may increase the difficulty of planning preclinical studies using longitudinal micro-CT scans [12–14]. Therefore, it is important to reduce radiation dose while striving to provide the highest image quality for small animal micro-CT.

Several techniques have been proposed to reduce the radiation dose, such as x-ray flux reduction [15, 16], sparse-view acquisition [17–19], and interior ROI imaging techniques (including theoretically-exact interior tomography [20–23] and other approximate-reconstruction-based ROI CT techniques [24–28]). X-ray flux reduction and sparse-view acquisition are readily applicable to the existing commercial / laboratory micro-CT scanners [29]. Noise and artifacts caused by x-ray flux reduction and sparse-view acquisition can be reduced by advanced reconstruction algorithms such as the ones based on compressive sensing and/or statistical modeling [15–19]. On the other hand, interior ROI imaging techniques require physical modification of system and/or the scan protocols [23–28]. Briefly, an internal ROI receives primary exposure delivered through an aperture in a "pre-patient" x-ray collimator [23–25, 28], while the region outside the targeted ROI receives no primary exposure. Interior ROI imaging techniques have been shown to significantly reduce radiation dose in clinical CT systems. For instance, R. Chityala et al. demonstrated 85.7% total dose reduction in a C-arm system, by shielding 82% of original field-of-view (FOV) [27]. D. Bharkhada et al. demonstrated up to 58% radiation dose reduction in a clinical spiral CT [23]. L. Chen et al. even reported 77.3% dose reduction inside the ROI due to scatter reduction [26]. Moreover, interior ROI imaging techniques can be combined with x-ray flux reduction and sparse-view acquisition to further reduce the radiation dose delivered to the internal ROI [20, 22, 30]. A number of advanced reconstruction algorithms have been proposed to address the artifacts caused by data truncation in interior ROI imaging [20, 31–35]. The aforementioned research works suggest that interior ROI imaging may be applicable in micro-CT for radiation dose reduction.

Nevertheless, to the best of our knowledge, no collimator-based interior ROI imaging techniques have been physically implemented in micro-CT systems, and radiation dose reduction from interior micro-CT for preclinical imaging has not been experimentally demonstrated. Some commercial micro-CT scanners (*e.g.* Xradia scanners) can achieve interior tomography through limited detector FOV by multiple objective lens between the sample and the detector. However, the sample is still fully irradiated by a wide x-ray beam and hence it does not serve the purpose of radiation dose reduction. Previously, we have developed a dynamic micro-CT scanner that provides high temporal-spatial resolutions (15 msec and 6.2 lp/mm) by using a carbon nanotube (CNT) field-emission based x-ray source [36]. The CNT x-ray source is programmable for electronic control of x-ray emission, which enables flexible exposure control for cardiac and respiratory gated micro-CT imaging of free-breathing mice with no wasted radiation exposure [36]. The conventional global micro-CT mode was still used in that scanner. Interior ROI imaging can be applied to restrict the x-ray beam path through a small internal ROI (*e.g.* heart, lung tumor, *etc.*) in small animals while significantly reducing radiation exposure to the surrounding tissues. We anticipate that the integration of these two techniques (*i.e.* CNT dynamic micro-CT and interior ROI imaging) will lead to highest image quality and lowest radiation risk in small animal micro-CT imaging.

In this paper, we describe our work on the implementation of interior ROI imaging in a CNT x-ray source based dynamic micro-CT scanner, and demonstrate the high quality of interior ROI images with greatly reduced radiation dose. We explored several practical issues of CNT x-ray source based interior micro-CT, such as the geometric calibration with a small (10 mm) interior FOV, the high-precision alignment between interior FOV of the scanner and internal ROI of the object, and most importantly, the image quality and radiation dose reduction. This paper is organized as follows. In Section 2, we present the system overview, imaging experiments, and methods for image reconstruction and evaluation. In Section 3, we show the experimental results. In the last section, we discuss the results and conclude this study.

2. Methods

2.1. The CNT source based micro-CT system

The schematic system configuration and the physical system setup are shown in Fig. 1. Interior micro-CT was realized by placing a source collimator (*i.e.* pre-patient) between x-ray source and objects to reduce the FOV (*i.e.* from FOV2 to FOV1). The system mainly consists of a flat panel x-ray detector (Hamamatsu, Inc. Japan), a motorized gantry (Huber, Inc. Germany), an XYZ manual sample stage (Newport, Inc. USA), and an in-house-built CNT x-ray source. The detector element size is 50μm. The collimator is a 2 mm thick lead plate (with a circular 3.73 mm aperture) fixed on an XYR stage (Thorlab, Inc. USA). The CNT x-ray source was constructed by using the previous design [36]. The x-ray focal spot size is of 100 μm diameter. The cone angle of x-ray beam was reduced from 30° to 3°, by using the aperture collimator.

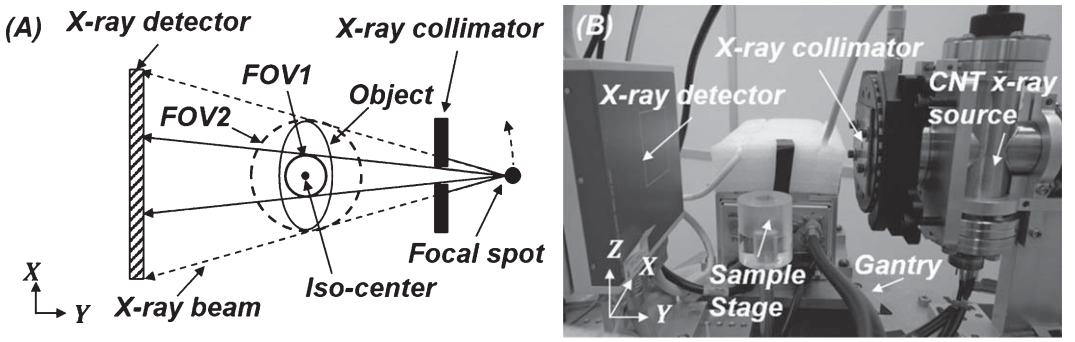

Fig. 1. (A) Schematic system configuration. FOV1 and FOV2 indicate the FOVs of interior micro-CT and global micro-CT, respectively. (B) Picture of the CNT interior micro-CT system.

Table 1
Parameters of imaging geometry and scanning protocols

Source-isocenter distance	167.8 mm
Source-detector distance	261.7 mm
Source-collimator distance	62.6 mm
X-ray tube voltage	50 kV
Exposure per projection	0.1 mAs
Scan angle	360°
Number of projections	720

During micro-CT scans, the object was stationary while the x-ray source and detector were rotated. The cone-beam circular trajectory was adopted for projection data acquisition. The step-and-shoot scan mode was employed to eliminate the motion blurring caused by continuous mechanical rotation of x-ray source and detector. The x-ray source was operated at 50 kV and filtered by a 0.5 mm aluminum filter. The diameters of the spherical FOV were 32 mm and 10 mm in global and interior micro-CT modes, respectively. The interior FOV is just slightly bigger than an adult mouse heart. The other major parameters of scan protocols and imaging geometry are summarized in Table 1. The system control software was developed under *LabVIEW* (National Instrument, Inc. USA).

2.2. Imaging experiments

The imaging experiments on two micro-CT phantoms and a mouse carcass were conducted to evaluate the image reconstruction quality (see Sec 2.5.1 for evaluation methods). The two micro-CT phantoms included a water phantom and a "multi-feature" phantom. The water phantom was an acrylic cylinder (25.5 mm diameter and 1.5 mm wall thickness) filled with water, with a sealed polypropylene tube (2.5 mm diameter and 0.15 mm wall thickness) placed in the center (Fig. 2A). Micro-CT images of the water phantom were used for Hounsfield Units (HU) calibration and CNR evaluation. The "multi-feature" phantom (diameter 20 mm) was fabricated by modifying the one used in our previous works [34, 35]. This phantom comprises of various attenuating materials such as acrylic tube, rubber granules, micro-pillar arrays, micro-capillary tubes, multi-bore tubing, electrical tapes and duct tapes (thickness range from 0.25 mm to 5 mm, see Fig. 2B). The "multi-feature" phantom was mainly used to evaluate interior ROI reconstruction with the presence of heterogeneous materials and fine structures. For the animal experiment, a euthanized adult C57 mouse (body length 110 mm and thorax diameter 25 mm) underwent an open-chest surgery to ligate all blood vessels from heart, and then 300μl iodine contrast agent (Omnipaque 350 mgI/ml) was injected into the heart chambers. The mouse carcass was frozen by using dry ice. The C57 mouse was chosen because it is a typical animal model widely-used in cardiovascular research. The ligation was used to retain the contrast agent in mouse heart. Micro-CT scans of the mouse heart *in situ* were conducted using the CNT interior micro-CT scanner. The interior ROI (9 mm in diameter) was targeted at the mouse heart. Two low-dose "scout view" projections (separated by 90° angular interval) of the mouse carcass were acquired at global micro-CT mode, to align the mouse heart with system isocenter. Another low-dose raw projection was acquired at interior micro-CT mode, to calibrate the aperture collimator and align the interior FOV with mouse heart. Both

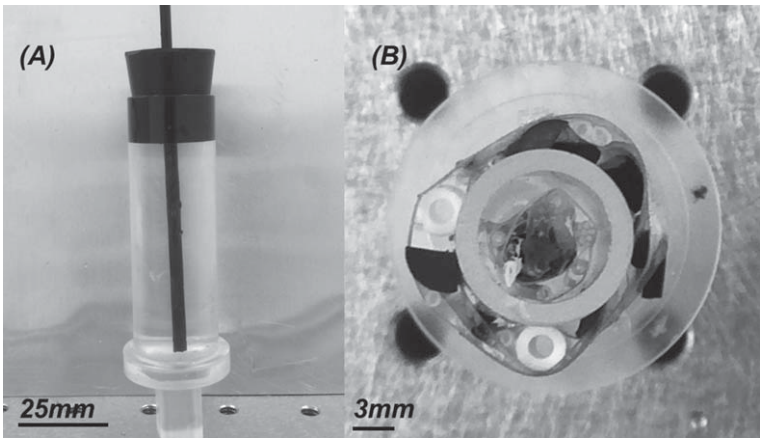

Fig. 2. In-house-built micro-CT phantoms for imaging experiments. (A) Side view of water phantom. (B) Top view of "Multi-feature" phantom.

global and interior micro-CT scans were conducted for each sample. The scanning protocol is listed in Table 1.

2.3. Image reconstruction

2.3.1. Geometric calibration and data preprocessing

System geometric calibration was conducted to identify the geometric parameters for accurate image reconstruction. Moreover, switching from global mode to interior mode could induce slight misalignment of interior FOV with the system isocenter, because of the mechanical tolerance of the aperture collimator. The analytic method proposed by F. Noo et al. [37] was adapted for geometric calibration of interior micro-CT. It is practical to assume that the collimator plane is parallel to system rotation axis and the detector plane. So, the geometric calibration of collimator can be accomplished by quantifying the in-plane offset (termed as "interior detector offset"). Interior detector offset can be calculated using interior projections (*i.e.* raw projections acquired at interior micro-CT mode). Figure 3 demonstrates the geometric calibration of interior detector offset. The projection of the collimator was not exactly circular because of unsmooth edge (Fig. 3A). Therefore, a circular image mask (as marked by the dashed circle) was applied to the interior projections, and the pixel values outside the mask were set to zeroes (Fig. 3B). P_m is the center of image mask, and P_1 is the intercept point between the detector plane and the "piercing line" (*i.e.* the line connecting focal spot and isocenter). The offset (d_x, d_y) between P_1 and P_m is defined as the interior detector offset. Raw projections were preprocessed to remove detector defects and then subjected to blank and dark projection corrections.

2.3.2. Reconstructions

As to interior micro-CT mode, we utilized our previously published frequency-split displaced detector (FSDDR) reconstruction technique [34]. Briefly, FSDDR algorithm employs a frequency splitting strategy to combine the post-convolution weighting based filtered back projection method (PCW-FBP) with the weighted simultaneous algebraic reconstruction technique (WSART). PCW-FBP incorporates sinogram reflection, sinogram splicing, cosine extrapolation and offset-detector-weighting function to filtered back projection method [34]. For WSART, the conventional SART algorithm is adapted for detector offset, by multiplying the offset-detector-weighting function [34]. Furthermore, total variation minimization (TVM) and ordered subset (OS) were also combined with WSART to guarantee theoretically accurate solution [20]. Finally, the frequency splitting scheme was applied to combine low frequency components and high frequency components respectively from the reconstruction results of PCW-FBP and WSART. For volumetric reconstruction, a GPU-based acceleration technique was utilized to significantly reduce the computational time [38]. As to global micro-CT mode, the conventional FDK algorithm [39] was employed for image reconstruction (referred to as global-FDK-reference images). The reason is that the FDK algorithm is typically utilized as the surrogate truth in current micro-CT applications [17, 30]. In addition, FSDDR algorithm was also applied in global micro-CT

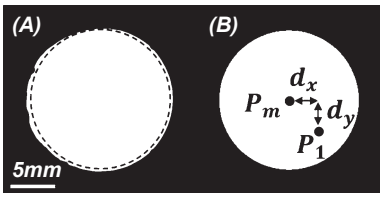

Fig. 3. Geometric calibration of interior detector offset. (A) The zoom-in interior blank projection. (B) The resultant projection after applying an image mask to subfigure (A). Note that the offset in (B) was exaggerated for illustration purpose. See detailed comments in Sec. 2.3.1.

mode (referred to as global-FSDDR-reference images) in order to provide a complementary evaluation of image quality by excluding the influence from different reconstruction algorithms.

2.4. Evaluation methods

2.4.1. Image quality analysis

Interior micro-CT images were compared against the global micro-CT images. All reconstructed images were calibrated to Hounsfield unit (HU) scale by using water phantom datasets. Three image quality metrics were employed for the quantitative assessment, including CNR, root mean square error (RMSE) and mean structural similarity index (MSSIM). Water phantom datasets were used to evaluate CNR. As is shown in Fig. 4, two circular ROIs were respectively selected from air region (*i.e.* ROI1) and water region (*i.e.* ROI2) to calculate CNR. The CNR is defined as follows [40, 41]:

$$CNR = \frac{|\mu_1 - \mu_2|}{\sqrt{\sigma_1^2 + \sigma_2^2}} \tag{1}$$

where μ_1 and μ_2 are respectively the average pixel value from ROI1 and ROI2, σ_1^2 and σ_2^2 are the corresponding variance. RMSE and MSSIM were calculated for all datasets to evaluate reconstruction accuracy. The RMSE is defined as follows:

$$RMSE = \sqrt{\frac{\sum |g(x, y) - f(x, y)|^2}{N}} \tag{2}$$

where N is the number of image pixels within the entire interior FOV, $g(x, y)$ is a pixel from interior micro-CT images, and $f(x, y)$ is the counterpart from global micro-CT images. The MSSIM is defined as follows [42]:

$$MSSIM = \frac{1}{M} \sum_{j=1}^{M} \left[l\left(x_j, y_j\right) \right]^{\alpha} \left[c\left(x_j, y_j\right) \right]^{\beta} \left[s\left(x_j, y_j\right)^{\gamma} \right] \tag{3}$$

where M is the number of local windows, x_j and y_j stand for the two groups of pixels in the *jth* local window from global micro-CT images and interior micro-CT images respectively, $l\left(x_j, y_j\right)$, $c\left(x_j, y_j\right)$, and $s\left(x_j, y_j\right)$ are respectively the comparison function for luminance, contrast, and structure. α, β and γ are parameters for adjusting relative importance of three comparison functions. These parameters were fixed at the same values in [42].

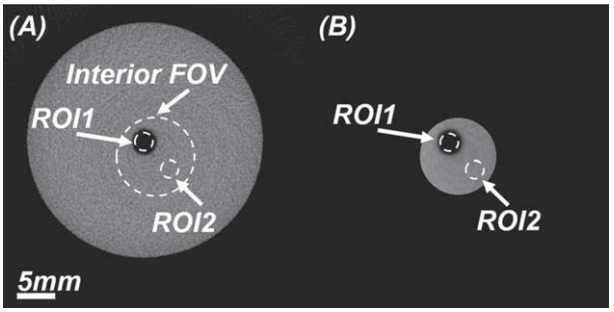

Fig. 4. Position of ROIs for CNR evaluation in water phantom datasets. ROI1 - air region. ROI2 - water region. (A) Global micro-CT image. (B) Interior micro-CT image. The region outside FOVs was cropped out by using image support. Display window [–1000 1000] HU.

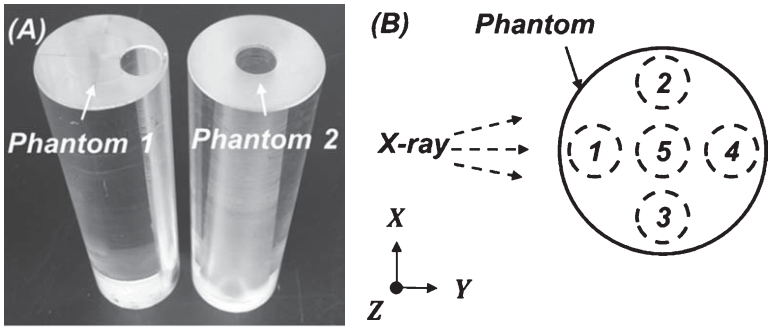

Fig. 5. (A) The in-house-built micro-CT dose phantoms. (B) Schematic five positions (top view) where ion chamber was placed in the phantoms.

2.4.2. Radiation dose measurement

We adapted the methods from the reference [23] to evaluate radiation dose reduction. Due to lack of standard phantom for micro-CT, we fabricated two acrylic micro-CT dose phantoms for radiation dose measurement (Fig. 5A). The diameter and the length of the phantoms were respectively fixed at 30 mm and 110 mm which were the approximate size of the commercial micro-CT dose phantom (QRM, Inc. Germany). One phantom has a peripheral bore hole (*i.e.* phantom 1) and the other has a central bore hole (*i.e.* phantom 2). Due to lack of small thermoluminescent dosimeters (TLD) and micro-ion chambers, a calibrated 100 mm pencil ion chamber (Model 10X5-3CT, *Radcal*, Inc.) was placed in the micro-CT dose phantoms to measure the accumulated radiation exposures at the five positions throughout the scans (Fig. 5B). The scan protocol in Table 1 was also used in the dose measurement. The phantom 2 was used to measure the radiation dose in the central position (*i.e.* position #5). The phantom 1 was used to measure the radiation dose in peripheral positions (*i.e.* positions #1 - #4). Note that phantom 1 was rotated to next position after radiation dose measurement was accomplished at current position.

We adopted the concepts of $CTDI_a$ from the references [43–45] to evaluate the average radiation dose across the nominal beam width. The formula of $CTDI_a$ is defined as follows:

$$CTDI_a = \frac{1}{a}\int_{-50mm}^{50mm} f(z)\,dz \tag{4}$$

where a is the nominal beam width along z-axis, and $f(z)$ is the radiation dose profile along z-axis. The weighted $CTDI_a$ is calculated as follows:

$$CTDI_{a,w} = \frac{2}{3}CTDI_a^{periphery} + \frac{1}{3}CTDI_a^{central} \tag{5}$$

Where $CTDI_a^{periphery}$ is the average dose at peripheral positions, and $CTDI_a^{central}$ is the dose at central position. The dose length product (DLP) was employed as the descriptor of total dose [44]:

$$DLP = CTDI_{a,w} \times a \tag{6}$$

3. Experimental results

3.1. Imaging results

Figure 6 demonstrates the comparison between global-FDK-reference images and interior micro-CT images of water phantom. By visual inspection, FSDDR algorithm suppressed the

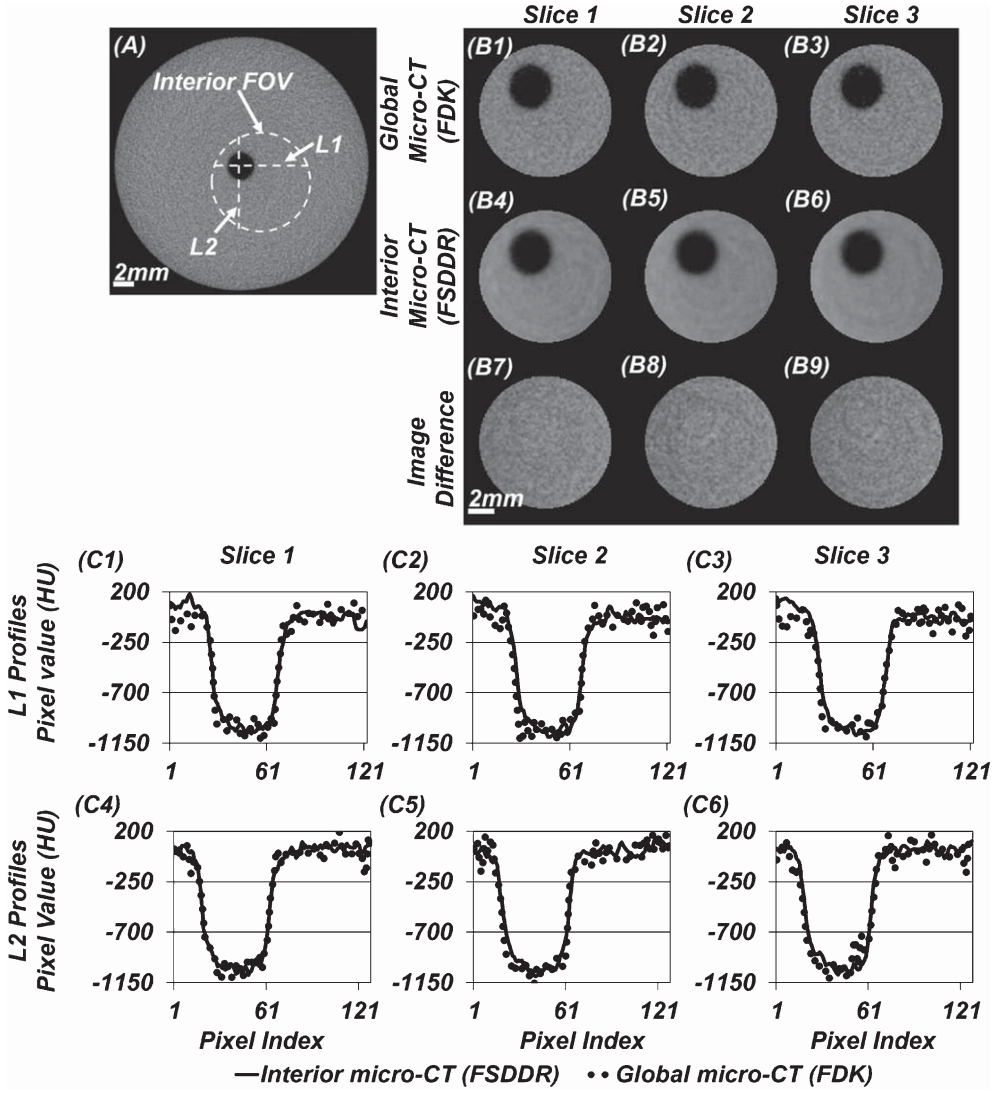

Fig. 6. The comparison between global-FDK-reference images and interior micro-CT images (axial slices) of water phantom. The region outside the FOV was cropped out by image support. (A) The location of interior FOV and line profiles. (B1-B3) Global micro-CT images. (B4-B6) Interior micro-CT images. (B7-B9) Image differences. Slice 2 is the central slice. Slices 1 & 3 are two off-mid-plane slices (0.26 mm away from the slice 2). (C1-C6) Line profiles from each slice. Display window is [–1000 1000] HU.

image noise of interior micro-CT images, while FDK algorithm yielded higher image noise in global micro-CT images. This is because FSDDR algorithm employs compressive sensing (CS) based iterative reconstruction technique which enables the noise reduction in piecewise constant type phantom. The image differences mainly demonstrated noise-like pattern. Table 2 demonstrated the value of CNR, RMSE and MSSIM from water phantom datasets. The mean CNR of global micro-CT images was 55% lower than that of interior micro-CT images. The mean RMSE of three slices was 103.5HU. High structural similarity index was observed as one would expect. The mean MSSIM of three slices was 0.9173.

Figure 7 demonstrated the comparison between global-FDK-reference images and interior micro-CT images of “multi-feature” phantom. By visual inspection, the low contrast line-shape structures at the bottom of interior micro-CT images are slightly weakened. This can be attributed to the TVM

Table 2
Quantitative quality metrics

		Global-FDK-reference images				Interior micro-CT images			
	Quality Metrics	Slice 1	Slice 2	Slice 3	Mean Value	Slice 1	Slice 2	Slice 3	Mean Value
Water phantom	*CNR*	8.83	9.35	8.77	8.98	20.13	20.44	19.08	19.88
	RMSE (HU)	–	–	–	–	99.28	104.1	107.11	103.50
	MSSIM	–	–	–	–	0.9191	0.9166	0.9162	0.9173
Multi-feature phantom	*RMSE (HU)*	–	–	–	–	150.48	150.50	153.74	151.57
	MSSIM	–	–	–	–	0.9346	0.9272	0.9263	0.9294
Mouse carcass	*RMSE (HU)*	–	–	–	–	572.75	580.75	609.79	587.76
	MSSIM	–	–	–	–	0.8663	0.8681	0.8527	0.8624

method which could reduce the image noise at the expense of smoothing out small structures [46]. Nevertheless, the high and low contrast structures of the phantom remain largely consistent in the images from both modes, and no significant artifacts are induced in interior micro-CT images. The image differences also mainly demonstrated noise-like pattern. The line profiles from interior micro-CT images were well-matched to those from global micro-CT images. Table 2 also demonstrated the RMSE and the MSSIM from multi-feature phantom datasets. High structural-similarity-index was still observed. The mean MSSIM of three slices was 0.9294. Despite the heterogeneous inner materials and the sub-millimeter structure, interior micro-CT images still presented high structural similarity to global micro-CT images.

Figure 8 presents the comparison between global-FDK-reference images and interior micro-CT images of mouse carcass. By visual inspection, FDK algorithm yielded visible streak artifacts in global micro-CT images, which was mainly induced by bony structure and iodine contrast agent. The streak artifacts had degraded image contrast. On the contrary, FSDDR algorithm suppressed the artifacts and enhanced the image contrast. The suppression of streak artifacts by the FSDDR algorithm could be attributed to the following reasons. First, CS based iterative reconstruction technique has been demonstrated to suppress streak artifacts [47, 48]. Second, the frequency splitting scheme allows adjusting the contribution of analytic reconstruction (*i.e.* PCW-FBP) and CS based iterative reconstruction (*i.e.* WSART). Briefly, it could combine less low frequency components from PCW-FBP with more high frequency components from WSART to constitute the reconstruction results of FSDDR algorithm, by using proper image filtering. More details can be referred to in reference [34]. Therefore, the streak artifacts could be reduced by using frequency-split scheme, although some amount of residual could be present. The image differences and line profiles demonstrated relatively larger discrepancy. Table 2 also demonstrated the RMSE and the MSSIM from mouse carcass datasets. The mean RMSE of three slices was 587.76HU. Despite higher RMSE, the structural similarity index was maintained at a relatively high level. The mean MSSIM of three slices was 0.8624. Figure 9 shows the comparison of other representative axial, coronal, and sagittal slices and volume rendering between interior and global-FDK-reference images. The anatomical structure such as blood vessels (as marked by solid arrows) and heart chambers still demonstrated high visual fidelity.

Figure 10 presents the comparison between global-FSDDR-reference images and interior micro-CT images of the three aforementioned samples. By visual inspection, global and interior micro-CT modes demonstrated comparable image quality in terms of image noise, contrast and structural similarity. In water phantom dataset, the CNR of global-FSDDR-reference image was 18.5, which was close to that of interior micro-CT images (see Table 2). Higher structural similarity index was also observed. The MSSIM was respectively 0.9330, 0.9614 and 0.8939 for water phantom, "multi-feature" phantom and mouse carcass.

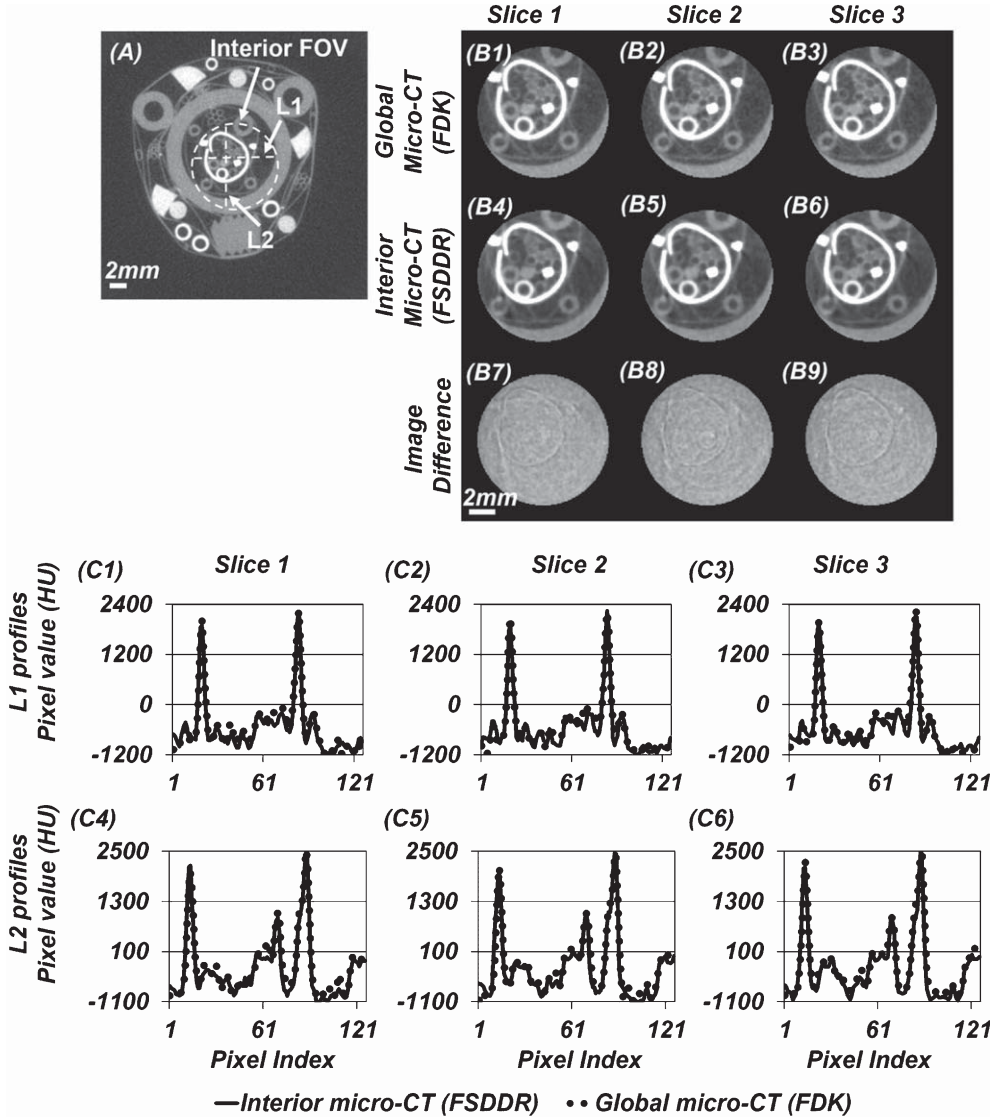

Fig. 7. The comparison between global-FDK-reference images and interior micro-CT images (axial slices) of multi-feature phantom. The region outside the FOV was cropped out by image support. (A) The location of interior FOV and line profiles. (B1-B3) Global micro-CT images. (B4-B6) Interior micro-CT images. (B7-B9) Image differences. Slice 2 is the central slice. Slices 1 & 3 are two off-mid-plane slices (0.26 mm away from the slice 2). (C1-C6) Line profiles from each slice. Display window is [–1700 1000] HU.

3.2. Radiation dose

The results of radiation dose measurement are demonstrated in Table 3. Interior micro-CT mode demonstrated significantly less radiation dose than global micro-CT mode. Significant dose reduction was observed at the peripheral positions (up to 65.9%). As is expected, the percentage dose reduction was higher at the peripheral positions than at the center (up to 8.6%). Unlike the central region, the peripheral region was only partially irradiated by the collimated x-ray cone beam during interior micro-CT scan. The dose reduction in both central and peripheral region leads to overall dose reduction. Compared with global micro-CT mode, interior micro-CT mode demonstrated significant percentage reduction of $CTDI_{a,w}$ (up to 48%) and DLP (up to 83.9%).

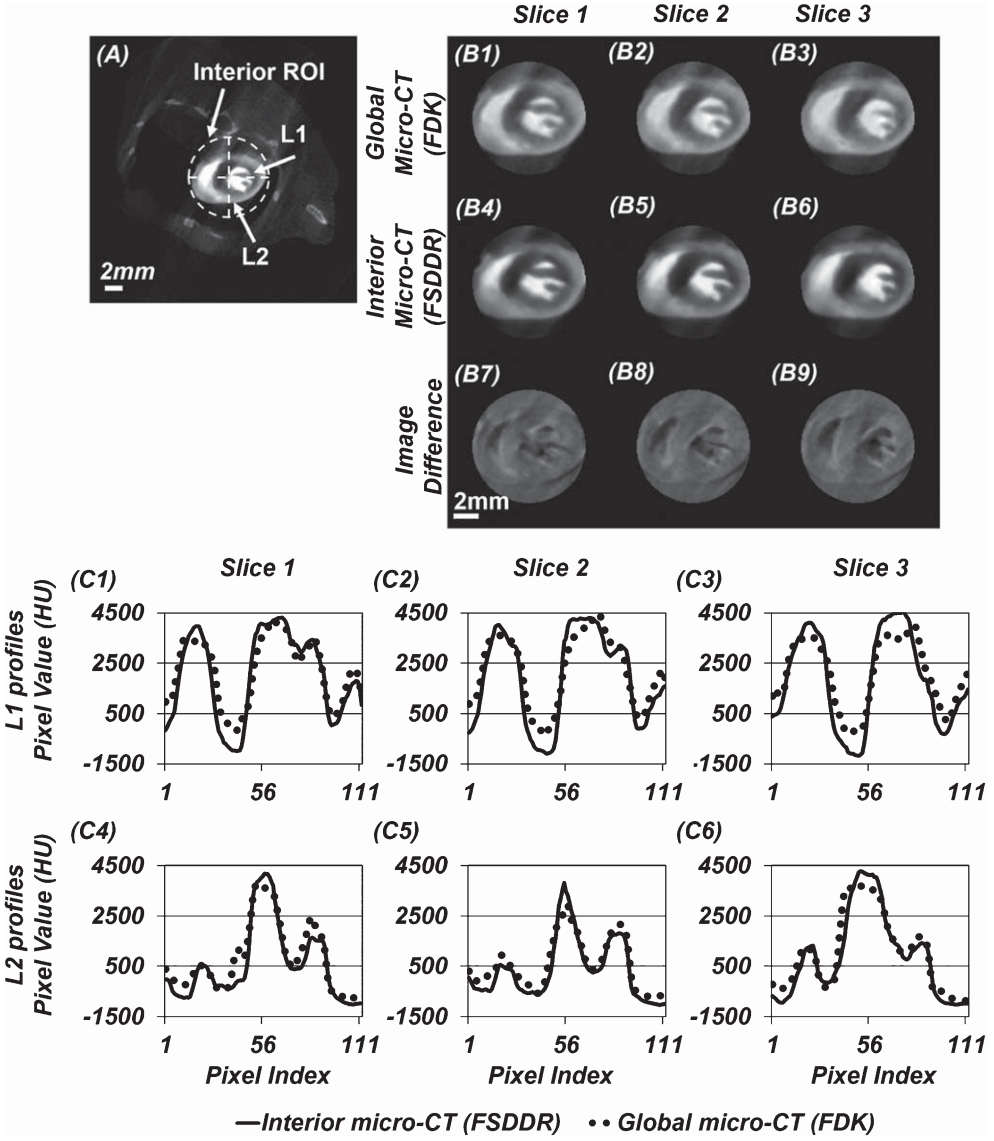

Fig. 8. The comparison between global-FDK-reference images and interior micro-CT images (axial slices) of mouse carcass. The region outside the ROI was cropped out by image support. (A) The location of interior ROI and line profiles. (B1-B3) Global micro-CT images. (B4-B6) Interior micro-CT images. (B7-B9) Image differences. Slice 2 is the central slice. Slices 1 & 3 are two off-mid-plane slices (0.26 mm away from the slice 2). (C1-C6) Line profiles from each slice. Display window is [–1500 4500] HU.

Table 3
$CTDI_a$ (cGy) at positions #1 - #5, $CTDI_{a,w}$ (cGy) and DLP (cGy-cm)

	#1	#2	#3	#4	#5	$CTDI_{a,w}$	DLP
Global micro-CT	16.340	16.275	16.189	16.297	14.135	15.562	37.706
Interior micro-CT	5.566	5.578	5.664	5.871	12.919	8.086	6.066
Percentage reduction (%)	65.9	65.7	65.0	64.0	8.60	48.0	83.9

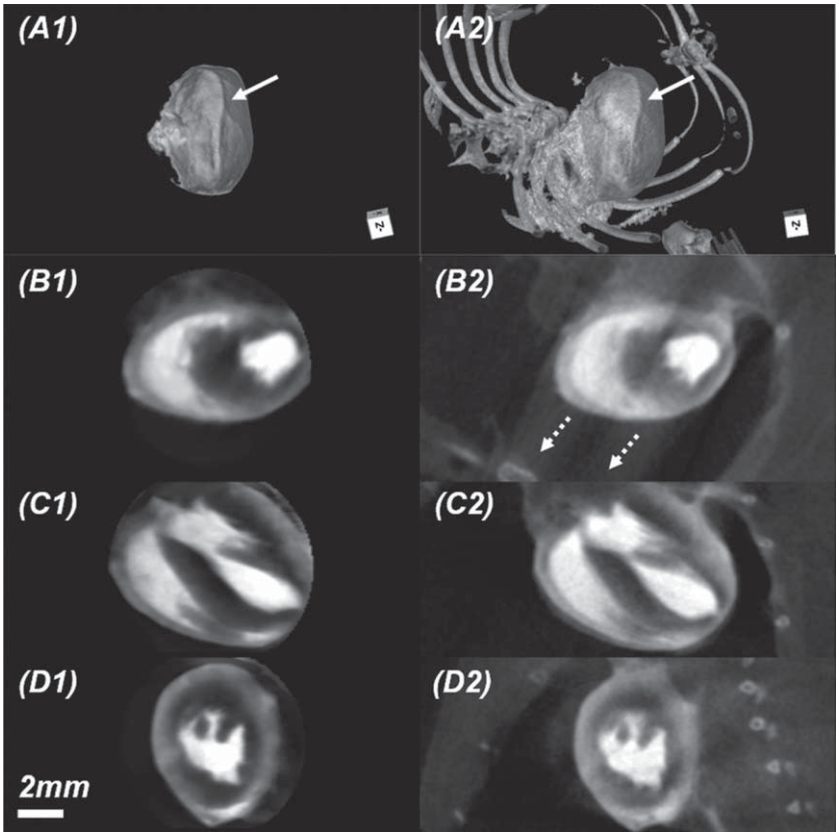

Fig. 9. The volume rendering and reconstructed images of mouse carcass. Left column: interior micro-CT images. Right column: global micro-CT images (FDK). (A1-A2): Volume rendering generated from *Volview* (Kitware, Inc. USA). (B1-B2) Axial slices. (C1-C2) Coronal slices. (D1-D2) Sagittal slices. The solid arrows in (A1-A2) indicate blood vessels. The dash arrows in (B2) indicate the direction of streak artifacts. Display window [–1500 4000] HU.

4. Discussion and conclusion

In this study, we used a source collimator to implement interior ROI imaging in a CNT x-ray source based micro-CT system. We conducted global and interior micro-CT scans on two micro-CT phantoms and a sacrificed mouse to evaluate the system performance. An iterative reconstruction algorithm (FSDDR) was employed for interior ROI reconstruction. Visual inspection and quantitative analysis were carried out to evaluate the image quality. Moreover, we experimentally measured and compared the radiation dose from global and interior micro-CT.

The influence of source collimators on interior ROI imaging has been overlooked in previous cone-beam CT studies [49]. As is reported by D. Xue et al. [49], the source collimator can induce non-negligible penumbra effects and reduction of primary x-ray field intensity in a clinical cone-beam CT, which mainly results from the off-focal-spot radiation and the large geometric magnification from collimator plane to detector plane. The similar effects were observed in our interior micro-CT system. Despite the same geometry magnifications for the global and interior micro-CT modes in our system, the central x-ray ray intensity dropped about 10% from the global mode to interior mode. We attributed this reduction of the central ray intensity to the aperture collimator at the source, which can reduce the off-focal-spot radiations. In interior micro-CT, the x-ray intensity of the primary field decreases radially from the center toward the edge (up to about 5%). This can be explained by the penumbra effects caused by the interior collimator. Overall, the changes of primary x-ray field intensity can result

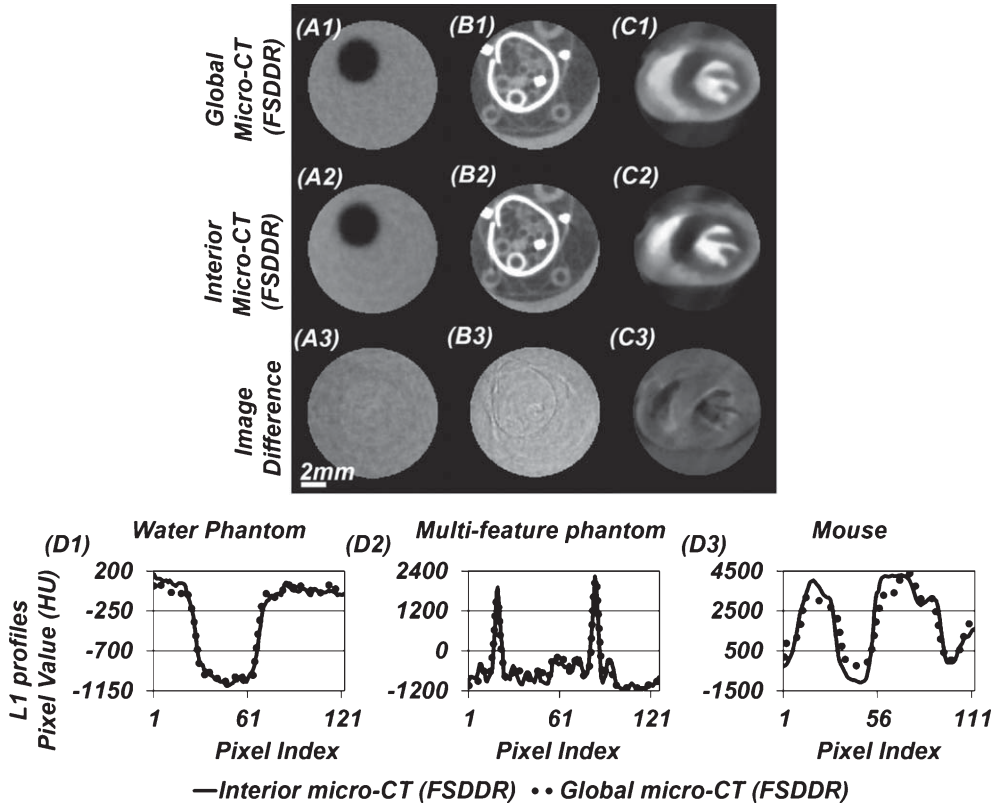

Fig. 10. The comparison between global-FSDDR-reference images and interior micro-CT images (central slices) of the three samples. (A1)-(A3) water phantom. (B1)-(B3) multi-feature phantom. (C1)-(C3) mouse carcass. Display window: (A1)-(A3) [–1000 1000] HU, (B1)-(B3) [–1700 1000] HU, (C1)-(C3) [–1500 4500] HU. (D1)-(D3) L1 line profiles from each slice. The locations of L1 line profiles are illustrated in Figs. 6–8.

in reconstruction error for interior ROI imaging [49]. To eliminate such error, interior raw projections have to be normalized by the corresponding interior blank projections in the preprocessing step.

The concept of CTDI was adopted as a micro-CT dose descriptor, because it has demonstrated linear response to the parametric changes of micro-CT scan protocols [45]. Moreover, CTDI was also used in dose measurement of interior clinical CT by D. Bharkhada et al. [23]. Furthermore, the concept of $CTDI_a$ was utilized instead of conventional $CTDI_{100}$, since our micro-CT system conducts cone-beam circular scans [44]. On the other hand, we have noticed that partial irradiation of ion chamber in interior micro-CT should cause some uncertainty to the measured $CTDI_a$ and DLP. Furthermore, the holes of 9.5 mm diameter may cause some uncertainties on dose measurement in the 20 mm to 30 mm diameter phantoms [50]. Nonetheless, our dose measurement should allow us to gauge the radiation dose reduction in this work.

In conclusion, we have demonstrated that interior ROI imaging can be implemented for radiation dose reduction in micro-CT imaging by mounting a source collimator. Using such a micro-CT scanner, we conducted comprehensive analysis of imaging quality and measured the radiation dose when the micro-CT system was applied for imaging physical phantoms and mouse carcass in both the conventional global micro-CT mode and the interior micro-CT mode. Interior micro-CT has been demonstrated to have comparable image quality to conventional global micro-CT, while significantly reducing radiation dose. We conclude that our CNT x-ray source based interior micro-CT system is applicable for high-quality and low-dose ROI-oriented preclinical imaging.

Acknowledgments

This work was partially supported by Dr. Cao's new faculty startup package at Virginia Tech, Drs. Cao and He's seed grants from Institute for Critical Technology and Applied Science at Virginia Tech, and Dr. Cao's CAREER support from the National Science Foundation (CBET 1351936). The work of Rui Liu and Hengyong Yu was partly supported by Dr. Yu's NSF CAREER award (CBET No. 1540898).

References

[1] E.L. Ritman, Current status of developments and applications of micro-CT, *Annual Review of Biomedical Engineering* **13** (2011), 531–552.

[2] A.Y. Sheikh, K.E.A. van der Bogt, T.C. Doyle, M.K. Sheikh, K.J. Ransohoff, Z.A. Ali, et al., Micro-CT for characterization of murine CV disease models, *JACC: Cardiovascular Imaging* **3** (2010), 783–785.

[3] R. Meuwissen and A. Berns, Mouse models for human lung cancer, *Genes Dev* **19**, (2005), 643–664.

[4] O. Engel, S. Kolodziej, U. Dirnagl, and V. Prinz, Modeling stroke in mice - middle cerebral artery occlusion with the filament model, *Journal of Visualized Experiments : JoVE* **2423** (2011).

[5] C.T. Badea, M. Drangova, D.W. Holdsworth, and G.A. Johnson, *In Vivo* Small Animal Imaging using Micro-CT and Digital Subtraction Angiography, *Physics in Medicine and Biology* **53** (2008), R319–R350.

[6] N.L. Ford, M.M. Thornton, and D.W. Holdsworth, Fundamental image quality limits for microcomputed tomography in small animals, *Medical Physics* **30** (2003), 2869–2877.

[7] R.A. Brooks and G. Di Chiro, Statistical limitations in x-ray reconstructive tomography, *Medical Physics* **3** (1976), 237–240.

[8] T. Ohnishi, A. Takahashi, K. Ohnishi, and M. Yonezawa, Tumor suppressor p53 response is blunted by low-dose radiation, *Phys Med* **17**(Suppl 1) (2001), 215–216.

[9] S.L. Chen, L. Cai, Q.Y. Meng, S. Xu, H. Wan, and S.Z. Liu, Low-dose whole-body irradiation (LD-WBI) changes protein expression of mouse thymocytes: Effect of a LD-WBI-enhanced protein RIP10 on cell proliferation and spontaneous or radiation-induced thymocyte apoptosis, *Toxicological Sciences* **55** (2000), 97–106.

[10] E. Flockerzi, S. Schanz, and C.E. Rübe, Even low doses of radiation lead to DNA damage accumulation in lung tissue according to the genetically-defined DNA repair capacity, *Radiotherapy and Oncology* **111** (2014), 212–218.

[11] D. Mathias, R.E.J. Mitchel, M. Barclay, H. Wyatt, M. Bugden, N.D. Priest, et al., Low-dose irradiation affects expression of inflammatory markers in the heart of ApoE -/- mice, *PLoS One* **10** (2015), e0119661.

[12] V. Kersemans, J. Thompson, B. Cornelissen, M. Woodcock, P.D. Allen, N. Buls, et al., Micro-CT for anatomic referencing in PET and SPECT: Radiation dose, biologic damage, and image quality, *Journal of Nuclear Medicine* **52** (2011), 1827–1833.

[13] R. Laforest, C. Waterson, S. Broski, and J. Lewis, Radiation dose considerations in tumor growth monitoring with CT, *Mol Imaging* **3** (2004), 288.

[14] K.M. Prise, New advances in radiation biology, *Occupational Medicine* **56** (2006), 156–161.

[15] W.P. Shuman, D.E. Green, J.M. Busey, O. Kolokythas, L.M. Mitsumori, K.M. Koprowicz, et al., Model-based iterative reconstruction versus adaptive statistical iterative reconstruction and filtered back projection in liver 64-MDCT: Focal lesion detection, lesion conspicuity, and image noise, *AJR Am J Roentgenol* **200** (2013), 1071–1076.

[16] Q. Xu, H. Yu, X. Mou, L. Zhang, J. Hsieh, and G. Wang, Low-dose x-ray ct reconstruction via dictionary learning, *Medical Imaging, IEEE Transactions on* **31** (2012), 1682–1697.

[17] X. Han, J. Bian, D.R. Eaker, T.L. Kline, E.Y. Sidky, E.L. Ritman, et al., Algorithm-enabled low-dose micro-CT imaging, *Medical Imaging, IEEE Transactions on* **30** (2011), 606–620.

[18] Y. Lu, J. Zhao, and G. Wang, Few-view image reconstruction with dual dictionaries, *Physics in Medicine and Biology* **57** (2012), 173.

[19] E.Y. Sidky, C.-M. Kao, and X. Pan, Accurate image reconstruction from few-views and limited-angle data in divergent-beam CT, *Journal of X-ray Science and Technology* **14** (2006), 119–139.

[20] H. Yu and G. Wang, Compressed sensing based interior tomography, *Physics in Medicine and Biology* **54** (2009), 2791.

[21] G. Wang and H. Yu, The meaning of interior tomography, *Physics in Medicine and Biology* **58** (2013), R161.

[22] Q. Xu, X. Mou, G. Wang, J. Sieren, E.A. Hoffman, and H. Yu, Statistical interior tomography, *Medical Imaging, IEEE Transactions on* **30** (2011), 1116–1128.

[23] D. Bharkhada, H. Yu, R. Dixon, Y. Wei, J.J. Carr, J.D. Bourland, et al., Demonstration of dose and scatter reductions for interior computed tomography, *Journal of Computer Assisted Tomography* **33** (2009), 967.

[24] Y. Shen, Y. Yi, Y. Zhong, C.J. Lai, X. Liu, Z. You, et al., High resolution dual detector volume-of-interest cone beam breast CT–Demonstration with a bench top system, *Med Phys* **38** (2011), 6429–6442.

[25] D. Kolditz, Y. Kyriakou, and W.A. Kalender, Volume-of-interest (VOI) imaging in C-arm flat-detector CT for high image quality at reduced dose, *Med Phys* **37** (2010), 2719–2730.

[26] L. Chen, C.C. Shaw, M.C. Altunbas, C.-J. Lai, X. Liu, T. Han, et al., Feasibility of volume-of-interest (VOI) scanning technique in cone beam breast CT—a preliminary study, *Medical Physics* **35** (2008), 3482–3490.

[27] R. Chityala, K.R. Hoffmann, S. Rudin, and D.R. Bednarek, Region of interest (ROI) computed tomography (CT): Comparison with full field of view (FFOV) and truncated CT for a human head phantom, *Proceedings - Society of Photo-Optical Instrumentation Engineers* **5745** (2005), 583–590.

[28] C.J. Lai, L. Chen, H. Zhang, X. Liu, Y. Zhong, Y. Shen, et al., Reduction in x-ray scatter and radiation dose for volume-of-interest (VOI) cone-beam breast CT–a phantom study, *Phys Med Biol* **54** (2009), 6691–6709.

[29] J. Bian, X. Han, E.Y. Sidky, G. Cao, J. Lu, O. Zhou, et al., Investigation of sparse data mouse imaging using micro-CT with a carbon-nanotube-based X-ray source, *Tsinghua Science & Technology* **15** (2010), 74–78.

[30] H. Yu, G. Cao, L. Burk, Y. Lee, J. Lu, P. Santago, et al., Compressive sampling based interior reconstruction for dynamic carbon nanotube micro-CT, *Journal of X-ray Science and Technology* **17** (2009), 295–303.

[31] E. Katsevich, A. Katsevich, and G. Wang, Stability of the interior problem with polynomial attenuation in the region of interest, *Inverse Problems* **28** (2012), 065022.

[32] H. Kudo, M. Courdurier, F. Noo, and M. Defrise, Tiny a priori knowledge solves the interior problem in computed tomography, *Physics in Medicine and Biology* **53** (2008), 2207.

[33] S. Tang, Y. Yang, and X. Tang, Practical interior tomography with radial Hilbert filtering and a priori knowledge in a small round area, *Journal of X-ray Science and Technology* **20** (2012), 405–422.

[34] K.S. Sharma, H. Gong, O. Ghasemalizadeh, H. Yu, G. Wang, and G. Cao, Interior micro-CT with an offset detector, *Medical Physics* **41** (2014).

[35] K.S. Sharma, C. Holzner, D.M. Vasilescu, X. Jin, S. Narayanan, M. Agah, et al., Scout-view assisted interior micro-CT, *Physics in Medicine and Biology* **58** (2013), 4297.

[36] G. Cao, L.M. Burk, Y.Z. Lee, X. Calderon-Colon, S. Sultana, J. Lu, et al., Prospective-gated cardiac micro-CT imaging of free-breathing mice using carbon nanotube field emission x-ray, *Med Phys* **37** (2010), 5306–5312.

[37] F. Noo, R. Clackdoyle, C. Mennessier, T.A. White, and T.J. Roney, Analytic method based on identification of ellipse parameters for scanner calibration in cone-beam tomography, *Physics in Medicine and Biology* **45** (2000), 3489.

[38] L. Rui, L. Yan, and Y. Hengyong, GPU-Based Acceleration for Interior Tomography, *Access, IEEE* **2** (2014), 757–770.

[39] L. Feldkamp, L. Davis, and J. Kress, Practical cone-beam algorithm, *JOSA A* **1** (1984), 612–619.

[40] M.E. Mullins, M.H. Lev, P. Bove, C.E. O'Reilly, S. Saini, J.T. Rhea, et al., Comparison of Image Quality Between Conventional and Low-Dose Nonenhanced Head CT, *American Journal of Neuroradiology* **25** (2004), 533–538.

[41] J. Stützel, U. Oelfke, and S. Nill, A quantitative image quality comparison of four different image guided radiotherapy devices, *Radiotherapy and Oncology* **86** (2008), 20–24.

[42] Z. Wang, A.C. Bovik, H.R. Sheikh, and E.P. Simoncelli, Image quality assessment: From error visibility to structural similarity, *Image Processing, IEEE Transactions on* **13** (2004), 600–612.

[43] R.L. Dixon and J.M. Boone, Cone beam CT dosimetry: A unified and self-consistent approach including all scan modalities–with or without phantom motion, *Med Phys* **37** (2010), 2703–2718.

[44] S. Kim, H. Song, E. Samei, F.-F. Yin, and T.T. Yoshizumi, *Computed tomography dose index and dose length product for cone-beam CT: Monte Carlo simulations* **12** (2011).

[45] M. Hupfer, D. Kolditz, T. Nowak, F. Eisa, R. Brauweiler, and W.A. Kalender, Dosimetry concepts for scanner quality assurance and tissue dose assessment in micro-CT, *Medical Physics* **39** (2012), 658–670.

[46] Z. Tian, X. Jia, K. Yuan, T. Pan, and S.B. Jiang, Low dose CT reconstruction via edge-preserving total variation regularization, *Physics in Medicine and Biology* **56** (2011), 5949–5967.

[47] Z. Zhu, K. Wahid, P. Babyn, D. Cooper, I. Pratt, and Y. Carter, Improved compressed sensing-based algorithm for sparse-view CT image reconstruction, *Computational and Mathematical Methods in Medicine* **2013** (2013), 15.

[48] X. Li and S. Luo, A compressed sensing-based iterative algorithm for CT reconstruction and its possible application to phase contrast imaging, *BioMedical Engineering OnLine* **10** (2011), 73–73.

[49] X. Dong, T. Niu, X. Jia, and L. Zhu, Relationship between x-ray illumination field size and flat field intensity and its impacts on x-ray imaging, *Medical Physics* **39** (2012), 5901–5909.

[50] J.M. Boone, O. Velazquez, and S.R. Cherry, Small-animal X-ray dose from micro-CT, *Molecular Imaging* **3** (2004), 149–158.